Submitted to the 29th International Conference on High-Energy Physics ICHEP98,
Vancouver, Canada, July 1998

Measurement of Neutral and Charged Current Cross-Sections at High Q^2

H1 Collaboration

Abstract

The inclusive single and double differential cross sections for neutral and charged current processes with Q^2 between 200 and 30000 GeV^2 are measured in e^+p collisions with the H1 detector at HERA using the data taken in 1994-1997, which corresponds to an integrated luminosity of 37 pb^{-1}. The data amount to an increase in statistics by a factor of twelve with respect to the analysis of the 1994 data alone. Substantial extension in the kinematic range towards high Q^2 and x has been achieved. The Q^2 evolution of the parton densities predicted by QCD is tested at large Q^2 and x-Bjorken values up to 0.65. Predictions of the electroweak theory are confronted with the data, and the mass of the W is extracted from the Q^2 dependence of the charged current cross-section.

Abstract: 533
Parallel sessions: 4,1
Plenary sessions: 6,1

1 Introduction

Deep inelastic scattering (DIS) of leptons off nucleons has played a fundamental role in the understanding of the structure of matter and the establishment of the Standard Model. A large number of experiments, carried out in the last three decades in the "fixed target" mode, have constrained the parton densities in the proton, and have stringently tested the predictions of Quantum Chromodynamics (QCD), the theory of the strong interaction which was developed following the first DIS results revealing the existence of partons in the proton [1]. Shortly afterwards, the electroweak theory was experimentally established with the observation of neutral currents in DIS of neutrinos in the CERN bubble chamber experiment [2].

At HERA, the first electron-proton collider ever built, the study of DIS has been further pursued since 1992 in new kinematic domains[1], both in neutral current (NC) in which a photon (γ) or a Z° is exchanged and in charged current (CC) in which the exchanged boson is a W [2]. With the 1993 data, the influence of the W on the CC cross-section was shown [3]. Since the majority of DIS events occur at low momentum transfer squared Q^2, emphasis was put in the first three years of operation on the region at low x in low Q^2 NC interactions, x being the Bjorken scaling variable. The measurements of the F_2 proton structure function revealed [4, 5] its strong rise with decreasing x and a behaviour which confirmed the predictions of perturbative QCD in the form of the Next-to-Leading Order (NLO) DGLAP [6] evolution equations.

First cross-section measurements in the high Q^2 ($\gtrsim 100$ GeV^2) region were achieved with the 1993 and 1994 data but the statistical precision of the data was insufficient to make stringent electroweak or QCD tests. Perturbative QCD was shown to be in agreement with the NC data up to $Q^2 = 5000$ GeV^2 [7, 8]. The ratio of the CC total cross-sections for e^-p and e^+p interactions was shown to be consistent with the results obtained in fixed target neutrino and antineutrino scattering and with the predictions of the Standard Model [9, 10]. The Q^2 dependence of the CC cross-sections $d\sigma/dQ^2$ was checked to be consistent with the Standard Model and used to determine the propagator mass M_W [11, 12].

From 1994 to 1997, the integrated luminosity has grown by about an order of magnitude, rendering a new measurement possible at high Q^2 with improved precision. The interest in the double differential cross-section measurement at the highest reachable Q^2 is increased by the observation with the 1994 to 1996 data by H1 and ZEUS [13, 14] of a possible excess of NC events at Q^2 greater than about 15000 GeV^2 compared with Standard Model expectations. In this article, the extension of the kinematic reach to higher x makes possible a more detailed comparison with the expected number of events at high Q^2, and probes directly the valence quark region. The precise measurement of the single and double differential cross-sections in a region in which the intermediate weak bosons play a significant role, tests the consistency of the electroweak theory in the t-channel, and constrains the basic electroweak parameters.

The paper is layed out in 4 main sections: after the introduction, the experimental technique used for the measurements is presented in section 2. In particular the kinematic reconstruction, the detector , the simulation, the data reduction, and the calibration are described. In section 3, the cross-section definitions and measurements, together with the systematic errors attached to them are presented. For NC and CC, the single ($d\sigma/dQ^2$ and $d\sigma/dx$) and double differential ($d^2\sigma/dxdQ^2$, and $d^2\sigma/dxdy$ for CC only) cross-sections have been measured and compared

[1]The positron and proton beam energies are 27.6 and 820 GeV. The center of mass energy is $\sqrt{s} = 301$ GeV

[2]At HERA, from April 1994 until the end of 1997 the collisions involved protons and positrons. In this paper, the word "electron" refers generically to electron and positron.

with the Standard Model. An extraction of the structure function F_2 is also presented with the Standard Model assumption for the longitudinal (F_L) and xF_3 structure functions. Section 4 is devoted to the interpretation of these results in the framework of the Standard Model. Studies of the validity of perturbative QCD at the highest $Q^2$and x and a measurement of the W mass in the t channel are presented.

2 Experimental Technique

2.1 Kinematics

The measurement of the differential DIS cross-sections relies on the precise determination of the kinematic variables associated with the interaction. For the charged current (CC) inclusive scattering process $ep \rightarrow \nu X$, these variables can only be reconstructed using the hadronic final state. For the NC case, the simultaneous reconstruction of the lepton and of the hadronic final state properties allows several complementary approaches to the kinematic reconstruction. In both cases, it is convenient to introduce the quantity Σ, the total transverse momentum $P_{T,h}$ and the inclusive hadronic angle γ defined by

$$\Sigma = \sum_h (E_h - p_{z,h}). \qquad P_{T,h} = \sqrt{(\sum_h p_{x,h})^2 + (\sum_h p_{y,h})^2} \qquad \tan\frac{\gamma}{2} = \frac{\Sigma}{P_{T,h}} \tag{1}$$

from which x, y and Q^2 are derived in the "hadron method". Here E_h and $p_{z,h}$ are the energy and longitudinal momentum component of a particle h, $p_{x,h}$, $p_{y,h}$, its components in the transverse plane. The summation is done over all hadronic final state particles and the masses are neglected. The formulae for the hadron (h) method are then given by [15]:

$$y_h = \frac{\Sigma}{2\,E_e} \qquad Q_h^2 = \frac{P_{T,h}^2}{1-y_h} \qquad x_h = \frac{Q_h^2}{s\,y_h} \tag{2}$$

This method is affected by particle losses in the beam pipe and by the fluctuations of the hadronic final state response of the detector. It is thus used only for the CC interactions.

The kinematic variables of the neutral current (NC) scattering process $ep \rightarrow eX$ can be reconstructed in different ways using measured quantities from the hadronic final state and from the scattered positron. The choice of the reconstruction method for Q^2 and y determines the size of systematic errors, acceptance and radiative corrections.

The method used in the NC measurement is the $e\Sigma$ method [16], which is a combination of the "electron method" and of the "Σ method" [16]. The electron method uses only the information of the scattered positron and has the best resolutions in x and Q^2 at large y, while the Σ method, which is calculated from the positron and the hadronic final state, has a good resolution over the entire kinematic range and is less sensitive to radiative corrections. The application and comparison of different methods yields a detailed understanding of the systematic errors associated with the measurement. In the $e\Sigma$ method, Q^2 is taken from the electron method, and x from the Σ method, since both these variables display excellent resolution in the complete kinematic range [17]. The formulae are simply obtained from $Q^2_{e\Sigma} \equiv Q^2_e$ and $x_{e\Sigma} \equiv x_\Sigma$, i.e.

$$Q^2_{e\Sigma} = \frac{E_e'^2 \sin^2\theta_e}{1-y_e} \qquad x_{e\Sigma} = \frac{E_e'^2 \sin^2\theta_e}{s\,y_\Sigma(1-y_\Sigma)} \qquad \text{with} \qquad y_\Sigma \equiv \frac{\Sigma}{E - p_z} \tag{3}$$

and $E - p_z \equiv \Sigma + E'_e(1 - \cos\theta_e)$ would be equal to twice the positron beam energy (55.2 GeV) in a perfect detector. The kinematics can also be reconstructed using the double-angle (DA) [18] method in which y and Q^2 are derived from θ_e and γ. The DA method has been mainly used for calibration purposes in this paper. At high Q^2 the differences between the methods tend to diminish, since, with increasing Q^2, the DA method improves, the hadronic final state is measured more precisely, and the low y region, in which the electron method is poor, slowly becomes kinematically inaccessible.

2.2 Detector and Trigger

The H1 detector [19] is a nearly hermetic multi-purpose apparatus built to investigate the deep inelastic scattering of electrons and protons at HERA. The high Q^2 structure function measurement relies primarily on the tracking chamber system, on the liquid Argon (LAr) calorimeter, on the luminosity detectors, and on a lesser extent on the backward calorimeter[3]. They are described briefly below.

The tracking system includes the central tracking chambers and the forward tracker modules. These chambers are placed around the beampipe at z positions between -1.5 and 2.5 m. A superconducting solenoid, which surrounds both the tracking system and the LAr calorimeter, provides a uniform magnetic field of 1.15 T. The central jet chamber (CJC) consists of two concentric drift chambers covering a polar angular range from $15°$ to $165°$. Tracks crossing the CJC are measured with a transverse momentum resolution of $\delta P_T/P_T < 0.01 \cdot P_T/\mathrm{GeV}$. To improve the determination of the z coordinate of the tracks, the CJC is supplemented by two cylindrical drift chambers at radii of 18 and 47 cm. A tracking chamber system made of three identical modules measures charged particles emitted in the forward direction ($7°$ to $20°$). The forward tracker is used to determine the event vertex for the events which leave no track in the CJC.

The scattered positron of the NC events and most of the hadronic final state energy are measured in the LAr calorimeter [20] which covers an angular region between $3°$ and $155°$. Some particle losses happen in the forward beam hole, which have an influence in particular on $P_{T,h}$ at low y. The calorimeter consists of an electromagnetic (e.m.) section with lead absorber plates and a hadronic section with stainless steel absorber plates. Both sections are highly segmented in the transverse and longitudinal directions with about 44000 cells in total. The electromagnetic part has a depth between 20 and 30 radiation lengths. The total depth of the calorimeter varies between 4.5 and 8 interaction lengths (λ_I). The electromagnetic energy uncertainty of the LAr calorimeter is determined to be less than 1%, obtained by a study of the "kinematic peak" in the positron energy spectrum at medium Q^2 ($100 < Q^2 < 1000$ GeV^2), and complemented at higher Q^2 by studies using further kinematic constraints as discussed in section 2.6.1. The hadronic energy uncertainty of the LAr calorimeter is determined to be between 3 and 4% by cross-calibration *in situ* with the scattered positron (see section 2.6.2).

In the backward region, a lead/scintillating fiber calorimeter (SPACAL) [21] was installed in 1995 to replace the previous lead/scintillator electromagnetic calorimeter (BEMC). The new calorimeter has both an electromagnetic and hadronic section with a total depth of about $2\lambda_I$. Its angular acceptance ($154° < \theta < 177.8°$) allows, in conjunction with the LAr calorimeter, for a quasi-complete containment of the hadronic final state. The hadronic energy scale uncertainty

[3]The positive z axis is defined at HERA as the incident proton beam direction.

of the measurement in the SPACAL is 7%, to be compared to 15% for the BEMC in 1994. However its influence on high Q^2 events is small.

The luminosity was determined from the measured cross section of the Bethe Heitler reaction $ep \to ep\gamma$. The final state positron and photon can be detected in calorimeters (electron and photon "taggers") close to the beampipe at large distances from the main detector (at $z = -33$ m and $z = -103$ m). For the final value of the luminosity only the hard photon Bremsstrahlung data were used. The precision of the luminosity determination is 2.6% [22].

The LAr calorimeter is used for the triggering of high Q^2 NC events, by means of the detection of a "tower" of electromagnetic energy pointing towards the event vertex [19] deposited by the scattered positron. Above the threshold energy of the analysis, 11 GeV, the trigger efficiency is greater than $99.5 \pm 0.5\%$. For CC events, since there is in general no compact shower in the calorimeter, the missing transverse momentum P_T^{miss}as reconstructed from the "towers" is used to trigger the event. At low P_T^{miss}in the backward region it is supplemented by a track based trigger for the 1997 data. The efficiency of the combination of these triggers reach an asymptotic value of $95 \pm 0.5\%$ for a missing transverse momentum P_T^{miss}above 25 GeV, and decreases smoothly to $50 \pm 5\%$ at the minimum $P_T^{\mathrm{miss}}$of the analysis (12 GeV).

2.3 Monte Carlo Simulation

Acceptance corrections and background contributions are studied with the data and Monte Carlo programs. DIS processes are generated using the DJANGO [23] event generator. The DJANGO program is based on HERACLES [24] for the electroweak interaction and on LEPTO [25] which uses the colour dipole model as implemented in ARIADNE [26] to generate the hadronic final state. HERACLES contains first order radiative corrections including real Bremsstrahlung process and virtual weak corrections. Based on the GEANT program [27] the detector response is then simulated in detail. After this step the Monte Carlo events are subject to the same reconstruction and analysis chain as the real data. The acceptance corrections for the NC events are performed after reweighting the simulated Monte Carlo events, produced with the MRSH [28] parton distributions, to the H1 QCD fit discussed in section 4 which gives the best description of the data. For the CC sample, no reweighting was performed.

The NC analysis makes use of an integrated Monte Carlo luminosity $\mathcal{L}_{MC} \approx 100$ pb^{-1}, i.e. about 3 times the luminosity of the data. For the 3 following regions, $Q^2 > 1000$ GeV^2, $Q^2 > 10000$ GeV^2 and $x > 0.3$ additional sets are used with $\mathcal{L}_{MC} \approx 700$ pb^{-1}, $\mathcal{L}_{MC} \approx 5$ fb^{-1} and $\mathcal{L}_{MC} \approx 700$ pb^{-1} respectively. For the CC analysis the simulated sample had a luminosity $\mathcal{L}_{MC} \approx 2.8$ fb^{-1}. An additional set for $Q^2 > 10000$ GeV^2 was used with $\mathcal{L}_{MC} \approx 63$ fb^{-1}.

The photoproduction background was simulated using the PYTHIA [29] generator for γp interactions. A sample of photoproduction events was generated and, after a preselection for being potential background events, the events were simulated in the detector. For the NC analysis the sample corresponds to 2.5 (5) times the data luminosity at low Q^2 for "resolved" ("direct") processes, and to 60 (120) times the data luminosity for $Q^2 > 5000$ GeV^2. The luminosity of the background sample for the charged current analysis is 1.5 (2.5) times the data luminosity for "resolved" ("direct") processes. The potential background originating from prompt photon production was studied on a simulated sample [30] representing 30 times the luminosity of the data.

Other physics processes which were found to give a small or negligible contamination have been studied:

- elastic and inelastic QED-compton processes are generated by the event generator EP-COMPT [31].
- $ep \to ep\, l^+\, l^-(eX\; l^+\; l^-)$: elastic and inelastic photon-photon processes producing pairs of leptons (l) are generated[4] using the LPAIR program [32].
- $ep \to eXW^{\pm}(eXZ)$: production of real heavy gauge bosons in DIS is generated by the EPVEC [33] event generator.

2.4 Data and Event Selection

The present analysis is based on the complete set of HERA data taken whilst colliding positrons and protons. The data were taken in the years 1994-1997 and correspond to an integrated luminosity $\mathcal{L} = 37.0$ pb^{-1}. The final DIS data sample comprises about 75000 NC events and 700 CC events [5].

The selection of high Q^2 NC and CC events is based on the identification of a scattered lepton with large transverse momentum, complemented with fiducial and kinematic cuts and the requirement of a reconstructed event vertex using central or forward tracks, lying within ± 35 cm of its nominal position.

In the case of CC events, the "identification of the neutrino" relies on the observation of missing transverse momentum ($P_T^{\rm miss}$) in the detector which is approximately the transverse momentum carried away by the neutrino which escapes detection. For the NC events, the lepton identification is positive and is based on the expected behaviour of a high energy positron in the H1 detector, namely

- The electromagnetic cluster of the candidate must be compact, with typically more than 70% of its energy concentrated in the 4 most energetic cells.
- The extrapolated trajectory of one of the charged track has a distance of closest approach to the center of gravity of the candidate cluster of less than 12 cm. The track is used for the polar angle (θ_e) measurement of the positron, while its momentum is more precisely derived from the calorimetric measurement. If $\theta_{cluster} < 40°$ this condition is not enforced, and the angle is determined from the cluster if there is no track pointing to it.

The fiducial cuts are applied only to the NC events, since they are made to preserve the quality of the positron reconstruction: the events are not considered in the analysis if their positron impact point in the calorimeter is in the limited regions with a large amount of inactive material (crack), as will be described in section 2.6.1. Similarly events are removed in which $\theta_e \gtrsim 153°$, since the scattered positron produces then an e.m. shower which is not fully contained in the calorimeter.

The kinematic cuts are made in order to avoid regions in which the measurement becomes experimentally difficult, or in which the background to signal ratio becomes important. These kinematics cuts are given for the NC and the CC events in table 1. In NC events, the $E-p_z$ cut reduces the background due to photoproduction and the size of radiative corrections. In CC events the V_{ap}/V_p cut reduces mainly the photoproduction background. It is defined and discussed in more details in section 2.5.1.

[4]Processes with $l^{\pm} = e^{\pm}$ can contribute to the NC sample, while in the CC sample processes with $l^{\pm} = \mu^{\pm}$ are more likely to contribute.

[5]The 1994 NC data ($\mathcal{L} = 2.7$ pb^{-1}) at $Q^2 \leq 5000$ GeV^2 already used in [7] are not used in this measurement.

Neutral Current	Charged Current
$E'_e > 11$ GeV	$P_T^{\mathrm{miss}}> 12$ GeV
$y_e < 0.9$	$0.03 < y_h < 0.9$
$E-p_z> 35$ GeV	$V_{ap}/V_p < 0.15$

Table 1: *Summary of event selection criteria for neutral current and charged current candidates. The V_p and V_{ap} quantities are defined in section 2.5.1*

2.5 Background Rejection

The background contribution to the DIS samples can be subdivided into ep-induced and non-ep-induced backgrounds. While ep-induced backgrounds are important in both the NC and CC analysis, non-ep backgrounds only contribute significantly to the CC sample. The latter mainly originate from cosmic rays or from secondaries from proton beam interactions.

2.5.1 ep-induced background

After all selection cuts, the only significant background in the NC sample is due to events from photoproduction processes in which the scattered positron escapes the detector along the beam pipe and one of the particles of the hadronic final state is misidentified as the scattered positron. The photoproduction background has been simulated and controlled using the subsample of about 10% of the events in which the scattered positron is detected in the electron "tagger". The remaining photoproduction background contribution to the neutral current sample is thus estimated and statistically subtracted from the final sample. It amounts in the complete sample to $\lesssim 1\%$ and at most 5% in the highest y bins at Q^2 below 1000 GeV^2. A conservative error of $\pm$ 30% is assigned to these numbers in the NC analysis.

Elastic QED-Compton events fulfil all the NC selection requirements and are not simulated in the DJANGO program. Such events, which represent less than 0.5% of the total sample are thus removed from the data sample once their topologic characteristics are recognized: they have exactly one reconstructed track, no hadronic activity in the calorimeters and no energy deposits in the remnant fragmentation region.

The main background for CC processes are photoproduction and NC events. Mismeasurement of energies and limited geometrical acceptance can in both cases lead to events which are not balanced in transverse momentum. For the rejection of this background two quantities V_p and V_{ap} are defined [34] from the vectorial transverse momentum $\vec{P}_{T,i}$ of all the particles i:

$$V_{p(ap)} \equiv (-) \sum_i \frac{\vec{P}_{T,h} \cdot \vec{P}_{T,i}}{P_{T,h}} \qquad \text{for} \qquad \vec{P}_{T,h} \cdot \vec{P}_{T,i} > (<) 0 \tag{4}$$

with $\vec{P}_{T,h} = \sum \vec{P}_{T,i}$, where the summation is over all particles of the event. These two variables quantify the transverse energy flow along the direction of the outgoing neutrino (V_{ap}) and in the opposite hemisphere (V_p). In CC events the energy flow is concentrated in the hemisphere opposite to the transverse momentum of the scattered neutrino, resulting in a low value for V_{ap}/V_p while in photoproduction and NC events it is more isotropic, i.e. giving values of V_{ap}/V_p close to 0.5. This can be seen in fig. 1a where V_{ap}/V_p is shown for photoproduction events where the scattered positron is tagged in the luminosity system and which pass the CC selection apart from the cut on V_{ap}/V_p, compared to Monte Carlo simulation. It is well described in shape and normalization. The number of events at low values of V_{ap}/V_p exceeding the expectation is consistent with random overlap events from Bethe-Heitler processes and CC events. The cut value on V_{ap}/V_p is 0.15 and the distribution of this variable for the events in the final data sample is well described by the combination of simulated DIS and photoproduction Monte Carlo events on either side of this value, as can be seen from fig. 1b. The remaining contamination of photoproduction events in the final CC sample is below 1%, an uncertainty of 50% on the photoproduction background is assigned for the CC analysis.

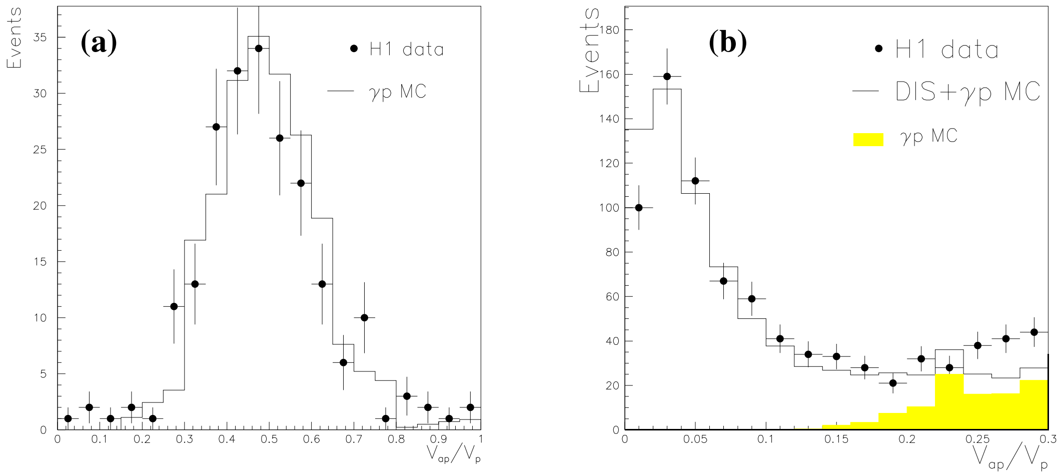

Figure 1: *Distribution of V_{ap}/V_p a) for tagged photoproduction events passing the CC selection except for the V_{ap}/V_p cut. b) for DIS events and simulated γp events passing the CC selection except for the V_{ap}/V_p cut. The complete simulation (histogram) normalized to the luminosity is compared to the data (points).*

Applying the NC selection on the final CC sample, a few events with a clearly isolated scattered positron candidate were observed, which are thus rejected from the CC sample. CC candidates with a high P_T lepton (e or μ) have been studied independently [35] and are rejected from the final sample.

2.5.2 Non-ep background

The event selection criteria described above can be satisfied by proton beam halo muons and cosmic rays which can interact with the detector material and cause an electromagnetic shower. Such events are efficiently rejected by the requirement of an interaction vertex (section 2.4) and the event timing T_0 determined by the tracking system coinciding with the nominal time of the bunch crossings of the beams.

These cuts also reject background from protons interacting with residual particles in the beampipe (beam-gas events) or with the beam pipe (beam-wall events) which can contribute to the CC sample.

After these cuts there is still background from random coincidences between soft photoproduction events and cosmic rays or beam halo muons. This background is rejected by a set of topological finders, a subset of which was already used and described in [9]. This subset has been extended and improved to accomodate new detectors and to increase the rejection power in particular at lower values of $P_T^{\rm miss}$[36, 37, 38]. These finders reject events in which a muon is successfully reconstructed using information from the LAr and Spacal calorimeters, the CJC and the Instrumented Iron system. For the NC sample these finders are only applied for the events not well balanced in transverse momentum. The inefficiency in the CC selection introduced by these finders is controlled in two different ways. A visual scan of rejected events yielded an overall inefficiency for the charged current selection of $5 \pm 1\%$ consistent with a comparison of the inefficiency obtained from NC events in which the information originating from the scattered positron has been removed and CC Monte Carlo events. The inefficiency of the topological finders in the NC analysis is negligible.

The final contamination of non-ep induced background events on the CC sample of about 10% in the sample is rejected by visual scanning. Ambiguities as derived from independent scanning represent less than 10% of the rejected events.

2.6 Calibration and Alignment

At high Q^2, the scattered positron, as well as the hadronic final state, are mainly measured by the liquid Argon calorimeter. From the test beam data, the initial e.m. and hadronic energy scale were established with an uncertainty of about 3% for electrons and pions between of energy between 4 GeV and 205 GeV [39, 40]. These energy scales were verified in the structure function measurement performed on the 1994 data [7]. For the present cross-section measurement, the uncertainties and the calibration constants have been improved by an in situ calibration which makes use of the larger NC event sample.

2.6.1 Positron Energy Measurement

The measured positron energy is corrected for energy losses in the dead material in front of the calorimeter, which account for about one radiation length (X_0), as well as for losses in the cracks between the calorimeter modules in the z and ϕ directions. In order to limit the size of the corrections in the crack regions, fiducial cuts of $\pm$ 2° around a ϕ crack and $\pm$ 5 cm around the two most vertical cracks in the z-direction between the CB1 and CB2 and the CB2 and CB3 wheels are applied (see fig. 2 for the angular coordinates of these wheels).

In the region of 80° $< \theta_e <$ 155° (40° $< \theta_e <$80°) NC-events were selected if $y_\Sigma <$ 0.3 ($y_\Sigma <$ 0.5). For these y values the energy of the scattered positron is predicted precisely by the DA method ($E_{\rm DA}$) and compared with the direct measurement (E'_e). The mean value and the width of the obtained distributions of $E'_e/E_{\rm DA}$ are adjusted between the data sample and the Monte Carlo simulation. From the Monte Carlo simulation an additional correction factor of about 1% is required to correct the computed double angle energy to the "true" energy, taking into account effects from initial state radiation. Using the impact position of the positron in the LAr calorimeter measured with the central tracking system, finely segmented regions in the z and ϕ directions are defined for which the calibration constants were determined locally. The calibration coefficients vary typically by $\pm$ 1% around their average value, except in the regions affected by z-cracks, were the corrections may reach up to 8% [37]. The difference after this calibration between the energy response of the data and of the simulated events is always smaller than 0.5% outside the cracks. After the calibration, the positron energy scale was cross-checked using elastic QED-Compton events, for which the scattered positron and the radiated photon should be balanced in transverse momentum. As the positrons and photons in these events are of lower energy, this cross-check also constitutes a verification of the linearity of the energy scale. The two methods are found to be in good agreement (fig. 2). A conservative error of $\pm$ 1% on the e.m. energy scale of this region of the detector is assigned.

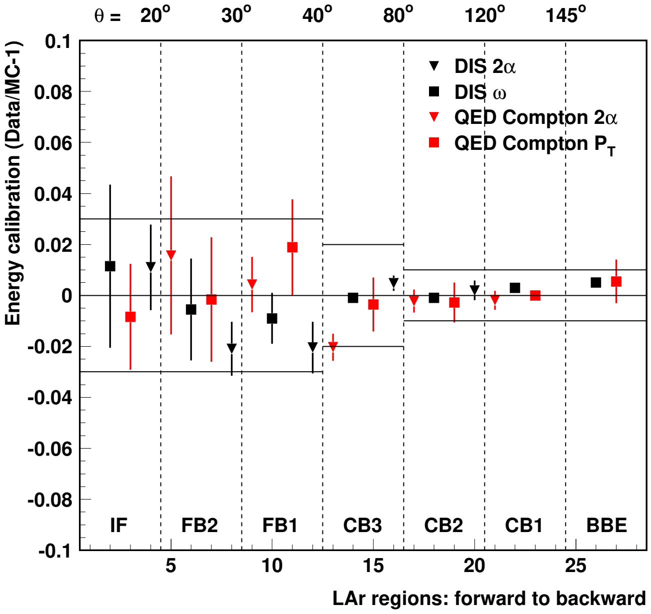

Figure 2: *Comparison of electromagnetic energy scale after in situ calibration from different methods.*

The limited statistics in the forward region ($\theta < 40^{\circ}$) do not allow such a fine calibration procedure to be performed. Therefore different methods have been compared and optimised in order to estimate the absolute energy scale. Using the NC event sample, the energy reconstructed with the double angle method, and the shift on the energy scale from the ω method [41], were determined. In the QED-Compton event sample the DA method and the comparison of the transverse momentum were studied. All these methods were cross-checked with the precise calibration in the backward region. The consistent picture of the various methods makes possible an improvement of the calibration constants of the forward calorimeter wheels at the percent level, with a remaining systematic uncertainty due to the low statistics of 3%. A summary of the calibration results is shown in fig. 2. The systematic uncertainties on the e.m. scale increase towards the forward region due to the lack of statistics, but no systematic trend is visible even at the highest Q^2. The resulting energy spectra are presented in figure 3b,c, and show a good description of the data sample by the simulation at all Q^2.

2.6.2 Positron Angle Measurement

The angle of the scattered positron is determined from the central tracking system ($\theta > 40^{\circ}$) or from the cluster position and the vertex position of the event ($\theta < 40^{\circ}$), with respect to the positron beam-position. The precision of the angle measurement with the tracking system (with the calorimeter) is better than 1 mrad (3 mrad). The vertex is determined from the tracking system with a precision of 1 cm in z and 1 mm in x and y. The mean position of the vertex depends

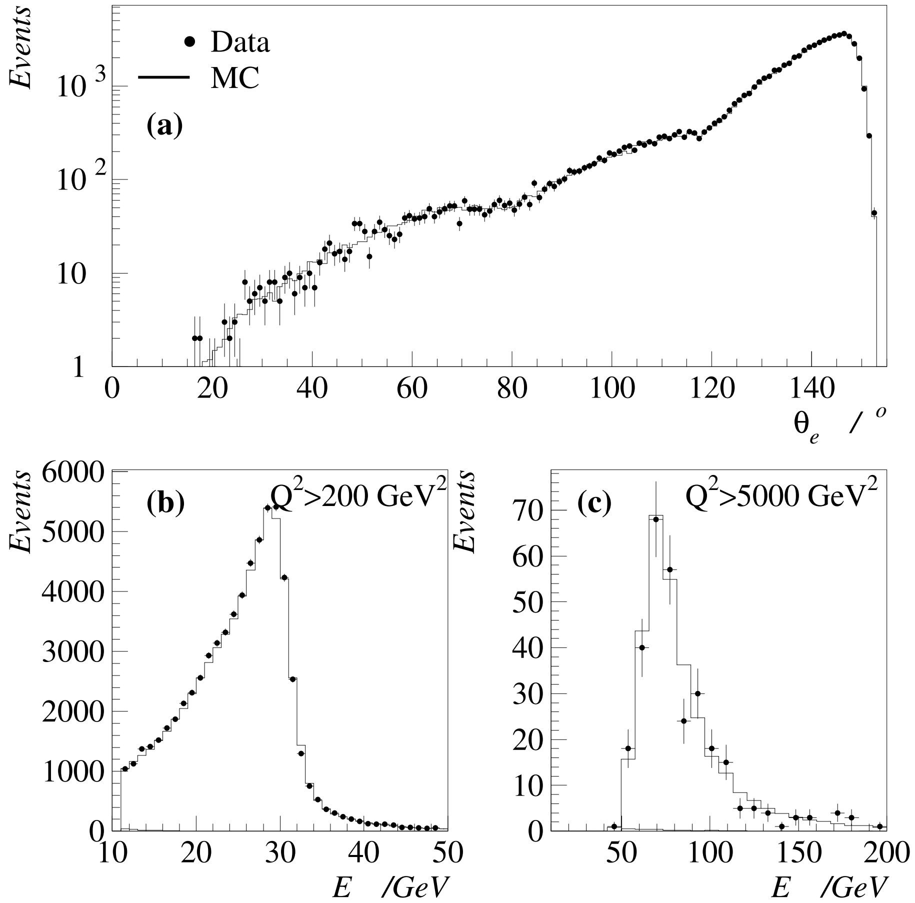

Figure 3: *a) θ distribution of the scattered positron. The irregular shape at $\theta_e \approx 120$ and $80°$ corresponds to two fiducial cuts. b) Energy spectrum of the scattered positron at Q^2 above 200 GeV^2, and (c) above 5000 GeV^2. The simulation (histogram) normalized to luminosity is compared to the data (points).*

on the proton beam-position which slightly varies when a new proton beam is injected. It is therefore determined for each proton filling, and the Monte Carlo simulation is then adjusted to it. The θ_e distribution is shown in fig. 3a. The irregular shape at $\theta_e \approx 80$ and $120°$ corresponds to the two fiducial cuts in between wheels mentioned in the previous section. The description of the data by the simulation is excellent even in these regions.

2.6.3 Calibration of the Hadronic Final State

As the H1 liquid Argon calorimeter is non compensating, weighting algorithms are applied to the hadronic clusters in order to improve the energy resolution [40, 42] beyond the dead material and crack corrections. In the central region of the calorimeter, a further improvement in resolution by about 10 to 20% for events having a $P_{T,h}$ between 10 to 25 GeV is obtained by using a combination of the energy of the low momentum tracks ($P_T < 2$ GeV) with the energy deposited by other particles of the hadronic final state in the calorimeter. To avoid double counting of the energy, the calorimetric energy in a cylinder of 20 to 40 cm in radius around the axis given by the direction of a low momentum track is not used in the sum [4]. The systematic uncertainty on the contribution to y_h from the track measurement is 3%. The contribution from the Spacal calorimeter to the y_h measurement is in general below 10% and only seen in events at high y. Its systematic uncertainty is 7%.

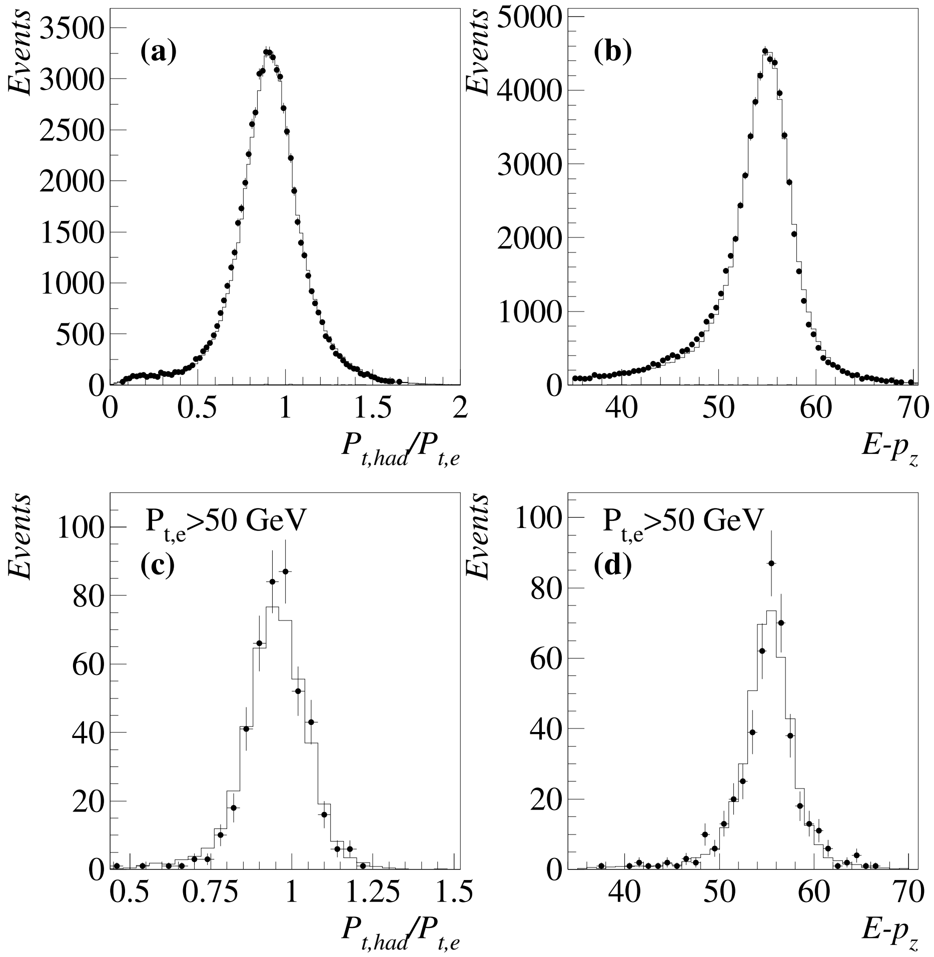

Figure 4: *a) Distribution of $P_{T,h}/P_{T,e}$ for the complete NC sample, c) for the subsample at $P_{T,e} > 50$ GeV. b) Distribution of $E-p_z$ for the complete NC sample, d) for the subsample at $P_{T,e}$ >50 GeV. The simulation (histogram) normalized to luminosity is compared to the data (points).*

For the calibration of the hadronic energy scale the transverse momentum of the precisely calibrated positron was compared to the transverse energy of the hadronic system. To localise differences in the calibration in the various parts of the detector, several techniques were developed allowing for a check of the calibration constants of the 56 electromagnetic and 64 hadronic octants from which the calorimeter is assembled. These procedures use either the positron in order to compute the inclusive hadronic angle and thus "predict" the direction of the current jet and the maximum amount of transverse energy in the hadronic final state, or unpack via the composition of $P_{T,h}$ a correlation matrix equation between the various octants, which is solved iteratively. The resulting coefficients from the two methods have been shown to be in good agreement, and justify a systematic error on the hadronic energy scale in the calorimeter of 3% in the forward part of the calorimeter and 4% in its backward part ($z < +100$ cm).

The measurement of the cross-section at low $y \lesssim 0.05$ is sometimes distorted by the presence of noisy calorimeter cells due to the electronics readout, or from the backscattering of particles from the proton remnant into the calorimeter. Both effects are included in the simulation, but need an efficient reduction in order to reach the required purity and stability criteria (cf section

3.2). Therefore additional noise-suppression algorithms were developed, based on the search for low-energetic isolated cells or clusters in the calorimeter. A systematic uncertainty of 25% of the subtracted noise was applied.

3 Cross-Section Measurements

3.1 Cross-Sections and Structure Functions

All the measured cross-sections presented in the following have been corrected for QED radiation effects. After this correction, the NC (CC) double differential cross-section is related to the initially measured cross-section via:

$$\frac{d^2\sigma_{NC(CC)}}{dx\;dQ^2} = \left(\frac{d^2\sigma_{NC(CC)}}{dx\;dQ^2}\right)_{init} (1+\delta^{qed}_{NC(CC)}(x,Q^2)) \tag{5}$$

The δ^{qed}_{NC} term includes the corrections due to photon emission from the lepton line, to the photonic lepton vertex corrections combined with the self energies of the external fermion lines [6], and to the fermion loops of the exchanged photon self energy. The δ^{qed}_{CC} term includes the leptonic part of the $\mathcal{O}(\alpha)$ photonic correction to CC processes [43, 44] and the self energy of the exchanged W. These radiative corrections are calculated using the HERACLES [24] (HECTOR [45]) program for the NC (CC) cross-sections. The purely weak corrections ($\delta^{weak}_{NC(CC)}$) as defined in [46] and which are small ($\mathcal{O}(1\%)$) have not been included. The Born cross-section is related to the measured cross-section via

$$\left(\frac{d^2\sigma_{NC(CC)}}{dx\;dQ^2}\right)_{Born} = \frac{d^2\sigma_{NC(CC)}}{dx\;dQ^2}\;\;(1+\delta^{weak}_{NC(CC)}(x,Q^2)) \tag{6}$$

The cross-sections which have been measured with the e^+p sample are:

- The single differential cross-section with respect to Q^2 (or x) which is labeled $d\sigma/dQ^2$ ($d\sigma/dx$). In these measurements the uncertainties are mainly coming from a possible smearing of events between one bin in Q^2 (x) and another, and from the event selection itself.

- The double differential cross-section which can be related to the proton structure functions or to the parton densities. For the NC case, the Born cross-section for $e^+p \to e^+X$ with unpolarized beams is proportional to a structure function term $\phi_{NC}(x,Q^2)$

$$\left(\frac{d^2\sigma_{NC}}{dx\;dQ^2}\right)_{Born} = \frac{2\pi\alpha^2}{xQ^4}\cdot\left[-y^2F_L(x,Q^2)+Y_+F_2(x,Q^2)-Y_-xF_3(x,Q^2)\right] \tag{7}$$

$$= \frac{2\pi\alpha^2}{x}\cdot\left(\frac{1}{Q^2}\right)^2\cdot\;\;\phi_{NC}(x,Q^2) \tag{8}$$

In this equation α is the fine structure constant, and the structure function term is a linear combination of the 3 following structure functions: the longitudinal structure function F_L , the F_2 structure function, and xF_3 which becomes significant only when Q^2

[6] The equivalent corrections from the quark side and the correction due to the lepton-quark interference are small and are included in the radiative correction systematic error.

is sufficiently large to render Z° exchange non-negligible. The helicity dependence of electroweak interactions is contained in the functions

$$Y_\pm = 1 \pm (1-y)^2. \tag{9}$$

According to QCD calculations the contribution of $y^2 F_L$ is small in the high Q^2 region, below 5% at the highest y of this analysis, and is negligible at lower y.

The structure function F_2 can be decomposed as

$$F_2 \equiv F_2^{em} + \frac{Q^2}{(Q^2+M_Z^2)} F_2^{int} + \left(\frac{Q^2}{Q^2+M_Z^2}\right)^2 F_2^{wk} = F_2^{em}(1+\delta_Z) \tag{10}$$

where M_Z is the mass of the Z° and F_2^{em} , F_2^{wk} and F_2^{int} are the contributions to F_2 due to photon exchange, Z° exchange and γZ° interference respectively.

In the kinematic range investigated the effect of the $\gamma - Z$ interference is smaller than 15% up to $Q^2 = 5000$ GeV^2, so that it is possible to extract F_2^{em} from the measured differential cross section. The difference between F_2 and F_2^{em} in the Standard Model is less than 1% for values of $Q^2 < 1000$ GeV^2. In the region of very high Q^2 (above 5000 GeV^2), the xF_3 term reduces significantly the e^+p cross section, so the determination of F_2 at these Q^2 relies on the calculation of xF_3 .

- The Born double differential CC cross-section can be expressed as in the NC case

$$\left(\frac{d^2\sigma_{CC}}{dx\,dQ^2}\right)_{Born} = \frac{G_F^2}{2\pi x} \cdot \left(\frac{M_W^2}{M_W^2+Q^2}\right)^2 \cdot \phi_{CC}(x,Q^2) \tag{11}$$

with G_F being the Fermi coupling constant, M_W the mass of the W boson and $\phi_{CC}(x,Q^2)$ the CC structure function term. In the special case of leading order QCD, and neglecting the effect of quark mixing, this cross-section is related to the quark parton densities (xu, xd, xs, xc) which are functions of x and Q^2:

$$\left(\frac{d^2\sigma_{CC}}{dxdQ^2}\right)_{LO} = \frac{G_F^2}{2\pi} \left(\frac{M_W^2}{M_W^2+Q^2}\right)^2 \left((\bar{u}+\bar{c}) + (1-y)^2(d+s)\right) \tag{12}$$

The NC and CC double differential cross-sections will be presented in the form of a so-called reduced cross-section in which in particular the propagator effects are diminished. The dependence of the cross-section on the structure function term, i.e. on the parton densities, becomes then more visible. For the NC case, the reduced cross-section $\tilde{\sigma}_{NC}$ is defined as

$$\tilde{\sigma}_{NC}(x,Q^2) \equiv \frac{x \cdot\; Q^4}{2\pi\alpha^2} \frac{1}{Y_+} \frac{d^2\sigma_{NC}}{dxdQ^2} \tag{13}$$

such that it coincides with F_2 in the region where xF_3 and F_L can be neglected. The reduced charged current cross section is defined in analogy with the NC one:

$$\tilde{\sigma}_{CC}(x,Q^2) \equiv \frac{x \cdot 2\pi}{G_F^2} \left(\frac{M_W^2+Q^2}{M_W^2}\right)^2 \frac{d^2\sigma_{CC}}{dxdQ^2} \tag{14}$$

Note that with this definition, apart for the small weak radiative corrections which have not been applied, the CC reduced cross-section is equal to the structure function term (see eq. 11), while the NC reduced cross-section has an extra $1/Y_+$ term.

3.2 Experimental Procedure

For the single or double differential cross-sections the measurement method is to convert, based on Monte Carlo acceptance calculations, the measured event numbers to a bin averaged cross-section, which is then corrected to the chosen bin center position. All detector efficiencies are determined from the data using the redundancy of the apparatus. They are correctly reproduced by the Monte Carlo simulation within the small errors quoted below, and therefore the simulation can be used to correct for the detector acceptance.

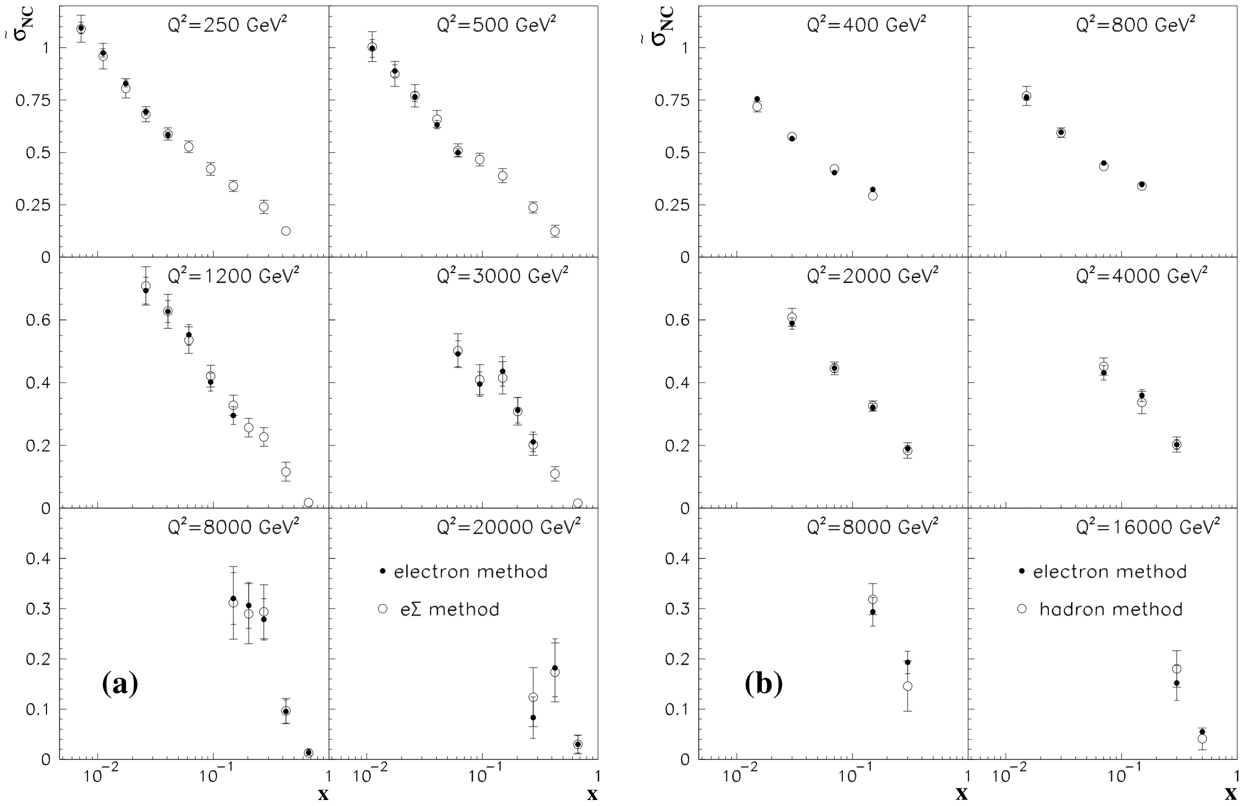

Figure 5: *Comparison of the reduced NC cross-section (as defined in eq. 13) measured (a) in the NC binning at six different Q^2 values, with the electron and eΣ method, and (b) in the CC binning with the electron and the h method. The good agreement shows the reliability of the detector calibration, and hence of the reduced NC and CC cross-section measurements presented in section 3.4.*

The NC data are binned in a $Q^2 - x$ grid, with 8 (5) bins per order of magnitude in Q^2 (x), except at $Q^2 > 3000$ GeV^2, for which a coarser bin in Q^2 is adopted to account for the rapidly decreasing number of events. The bins which are kept in this measurement have to satisfy two quality criteria which have been studied with the simulation. The stability and the purity [7] are both required to be larger than 30%. The quality of the kinematic reconstruction achieved can be judged by the comparison of the electron and the $e\Sigma$ method which is shown for 6 different Q^2 bins in fig. 5a. The good agreement between the two methods at high and medium y confirms the $e\Sigma$ result at low y, where the electron method is not usable.

[7]The stability (purity) is defined as the the fraction of events which originate from a bin and which are reconstructed in it, divided by the number of generated (reconstructed) events in that bin.

The same requirements are applied to the CC sample but for a coarser binning both in Q^2 (2 to 3 bins per order of magnitude) and in x (3 bins per order of magnitude) due to the inferior resolution of the hadrons-only reconstruction method used, compared with the $e\Sigma$ method used in the NC events. The reliability of the hadrons-only measurement in the chosen binning is demonstrated by the comparison of the measured NC reduced cross-section in the CC binning using the two independent methods ("electron" and "hadrons") as shown in fig. 5b.

3.3 Systematic Errors

The common list of systematic errors to NC and CC which have been considered is:

- An uncertainty of the positron energy of 1% if its impact on the calorimeter is in the backward part ($z_{imp} < 20$ cm), 2% for 20 cm $< z_{imp} < 100$ cm and 3% in the forward part ($z_{imp} > 100$ cm).
- An uncertainty up to 3 mrad for the positron polar angle.
- A 3% scale error for the hadronic energy in the forward part of the LAr calorimeter, and 4% in the remaining part. A 25% error on the noise subtraction in the LAr calorimeter.
- A 7% (3%) error on the energy of the hadronic final state measured in the SPACAL (tracking system).
- An error on the positron identification efficiency of 1% and an error on the track link requirement: 1%.
- An error on the vertex finding efficiency: 2%.
- An error on the trigger efficiency: 0.5% (NC), 0.5-5% for (CC)
- An error on the efficiency of non-ep background finders: 2%
- The uncertainty due to photoproduction background was assumed to be 30% (50%) of the correction applied for the NC (CC) measurement, i.e. smaller than 5%. This affects only the highest y bins.
- An error on the radiative corrections: 2% (NC), 4% (CC) [8].
- The luminosity error, averaged over the years, is presently 2.6%. It is not included in the systematic error bars of the measurements shown below.

Overall the typical total systematic error for the NC (CC) double differential cross-section is about 8% (15%).

[8] Improvements in the understanding of the CC radiative correction, in particular using the hadron method variables, are under study at the on-going workshop of "MC Generators for HERA Physics".

3.4 Single Differential Cross-Sections

The NC single differential cross-section $d\sigma/dQ^2$ is shown in fig. 6a. Also shown is a NLO QCD fit performed on the low Q^2 data which is described in section 4. The measurement spans more than two orders of magnitude in Q^2, and the rapid fall of the cross-section with Q^2 by about 6 orders of magnitude is well reproduced by the Standard Model (SM) prediction. Figure 6b shows the ratio of the measured cross section over the SM prediction. A slight excess of events is visible in the 2 highest Q^2 bins, which is less prominent than when studying the 1994 to 1996 data only [13]. Thus the 1997 data reduced the significance of the excess of events observed at high Q^2 by H1 with the previous data (see also [47]).

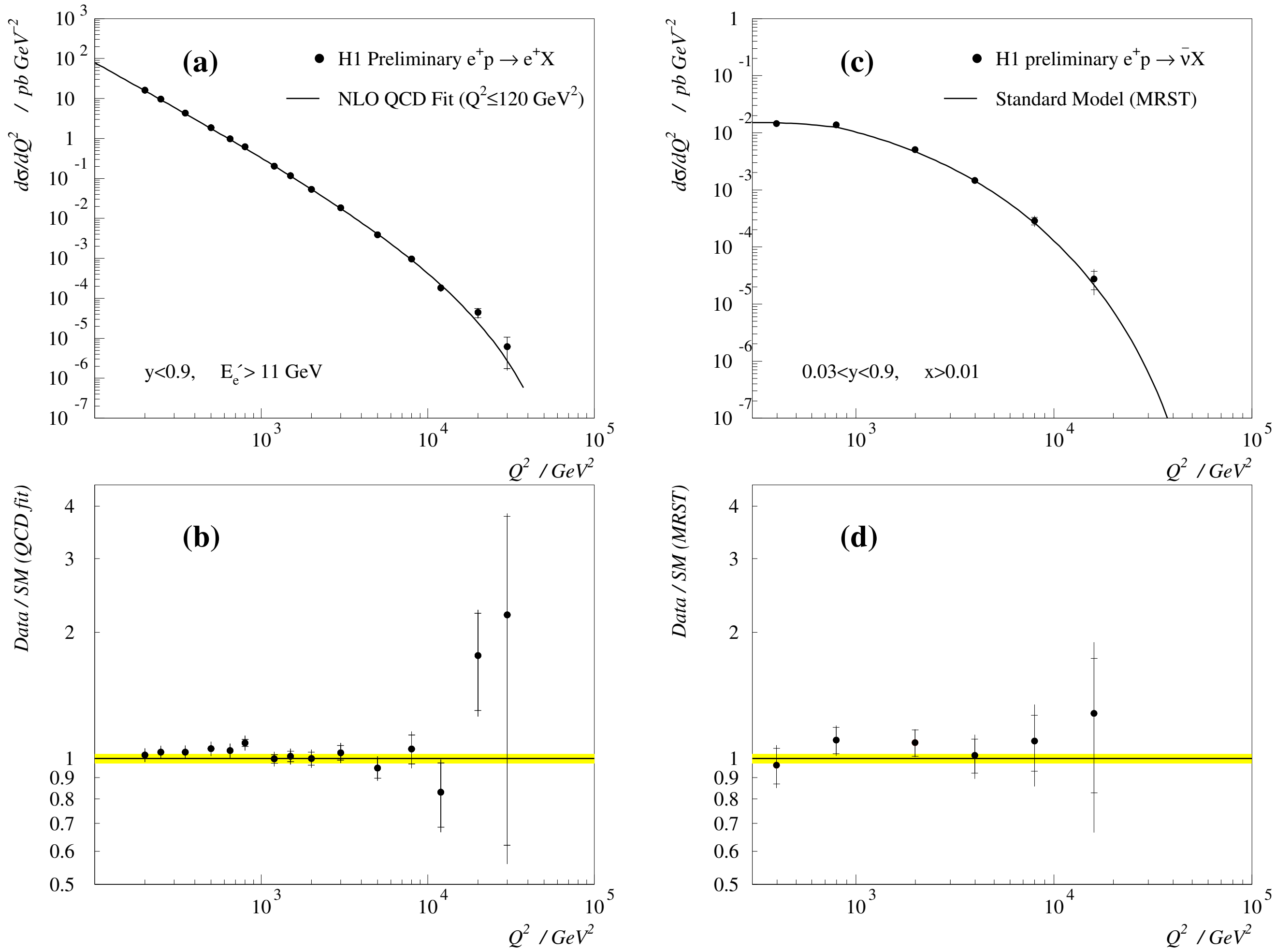

Figure 6: *a) The neutral current single differential cross section $d\sigma/dQ^2$ compared with the Standard Model prediction. b) The ratio NC cross-section divided by SM prediction. c) The CC single differential cross section $d\sigma/dQ^2$ compared with the Standard Model prediction. d) The ratio CC cross-section divided by the SM prediction. The gray band in b,d represent the present luminosity uncertainty of the measurement. The inner error bars represent the statistical errors, the outer ones correspond to the total error.*

In fig. 6c the corresponding cross-section is presented for the CC interactions. Due to the W mass term in the propagator, the fall of the cross-section is smaller, about 3 orders of magnitude. Both shapes and magnitude are well described by the SM prediction. The statistical uncertainty

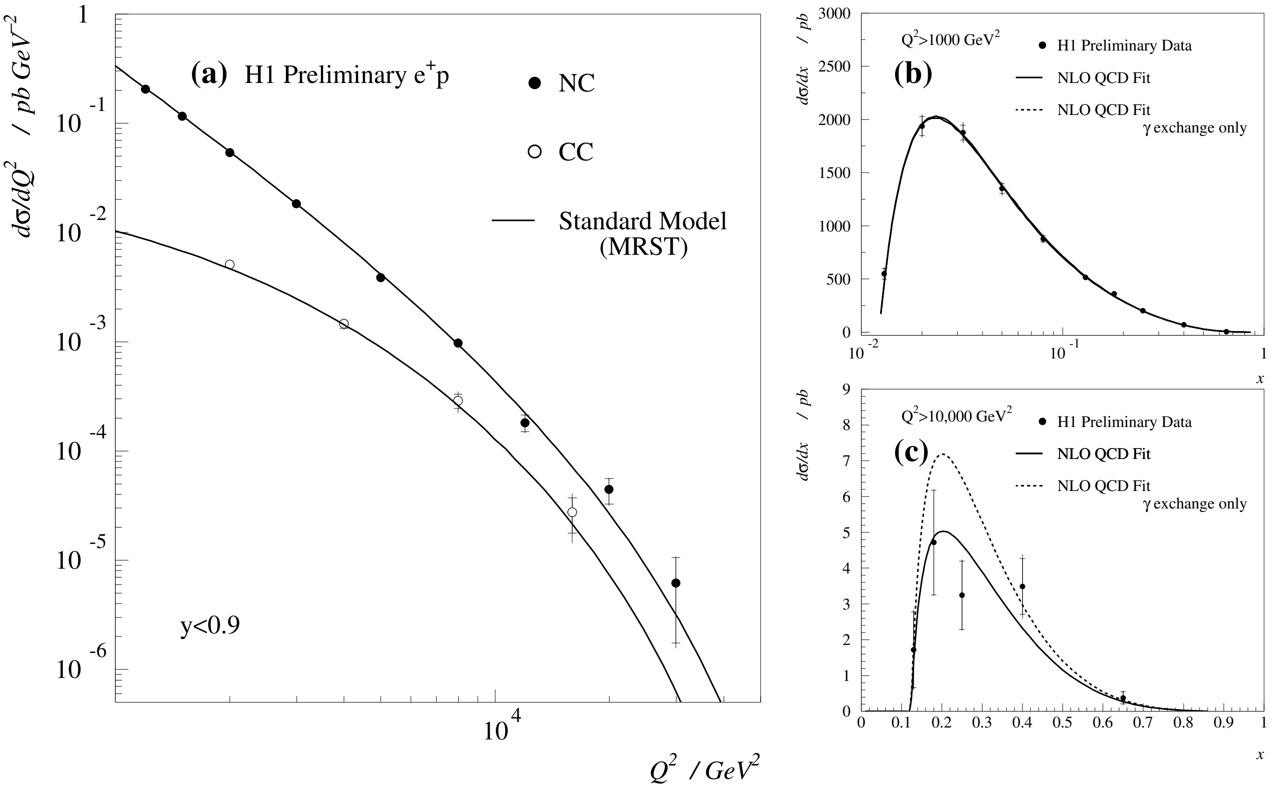

Figure 7: *a) Comparison of the neutral and charged current single differential cross section $d\sigma/dQ^2$ compared with the Standard Model predictions at high Q^2. b) The neutral current cross section $d\sigma/dx$ at high Q^2 compared with the Standard Model prediction and with the prediction when the coupling to the Z boson is not taken into account. The inner error bars represent the statistical errors, the outer ones correspond to the total error.*

is still the dominating factor at Q^2 above 5000 GeV^2 for NC interactions, and at all Q^2 for the CC interactions. The total systematic errors on these single differential cross-sections are about 4% in the NC case, and about 12% for the CC one.

The similarity at high Q^2 in shape and magnitude of these two single differential cross-sections, as predicted by the electroweak theory, is shown in fig. 7a for $Q^2 > 1000$ GeV^2.

The effect of the γZ interference is visible at HERA for the first time, as can be shown on the NC cross-section $d\sigma/dx$. In fig. 7b is shown the $d\sigma/dx$ cross-section at $Q^2 > 1000$ GeV^2. The measurement extends from $1.3 \cdot 10^{-2}$ to 0.65. The maximum of the distribution is obtained at $\approx 2 \cdot 10^{-2}$, i.e. at this low Q^2, the cross-section is still dominated by low x, "sea" partons (the sharp drop of the cross-section at $x < 2 \cdot 10^{-2}$ comes from the kinematic inaccessibility of this region at high Q^2). No difference in the prediction is observed with respect to the SM if only γ exchange is taken into account. In contrast, at $Q^2 > 10000$ GeV^2, as shown in fig. 7c, the two predictions are significantly different, and the data which have now their maximum in the valence region ($x \approx 0.2$), agree with the SM prediction and disagree at the 3 standard deviation level if only the γ exchange is taken into account.

3.5 Double Differential Cross-Sections

The NC reduced double differential cross-section is shown in fig 8, as a function of x at fixed Q^2 and compared to the H1 NLO QCD fit. At $Q^2 \lesssim 1000$ GeV^2 the total error is dominated

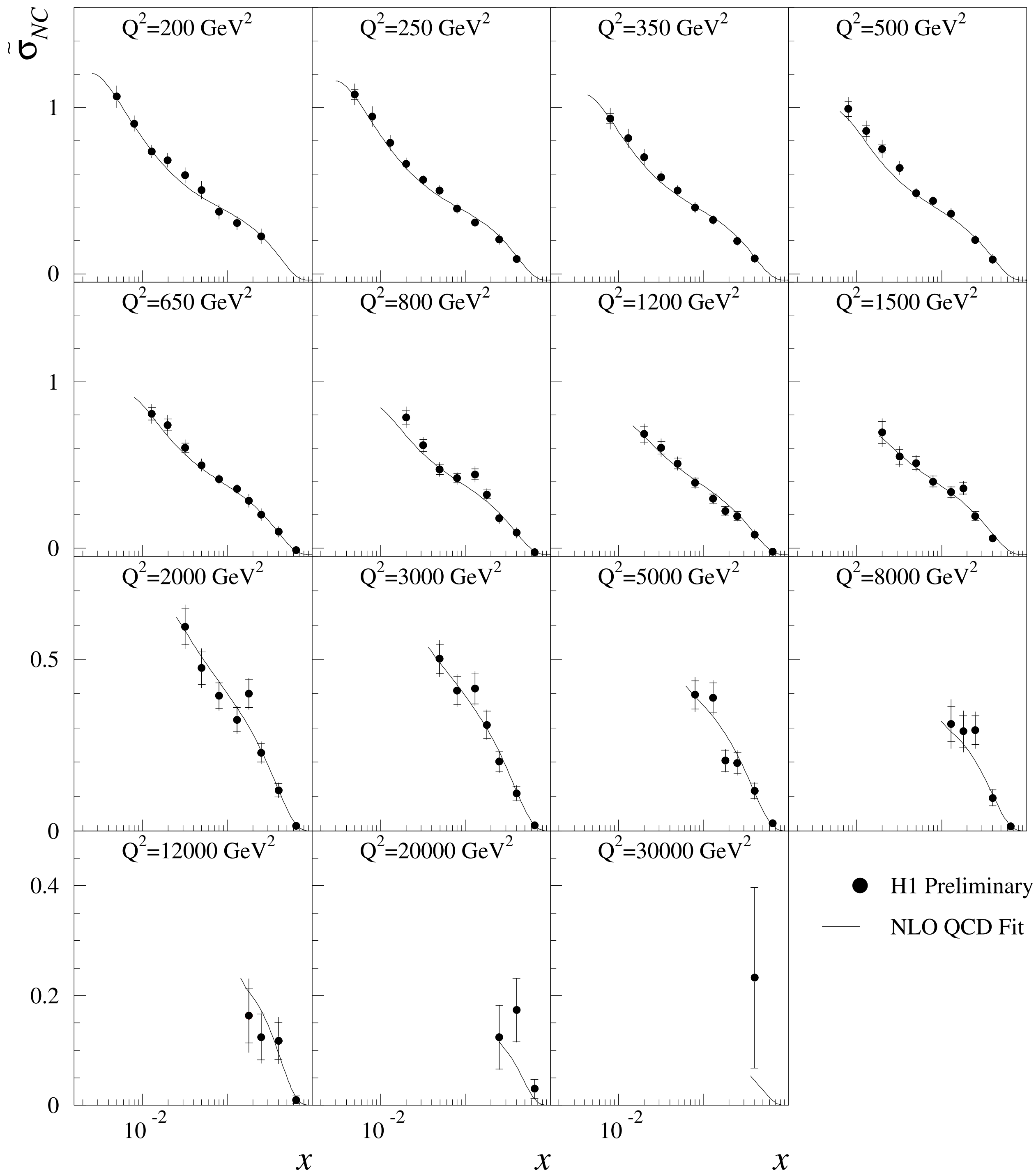

Figure 8: *The reduced neutral current cross section (as defined in eq. 13) as a function of x for different values of Q^2 compared with the NLO QCD fit described in section 4.1. The inner error bars represent the statistical errors, the outer ones correspond to the total error.*

by the systematic uncertainties, in particular from the uncertainty in the energy scales of the scattered positron and the hadronic final state. When going to higher Q^2, the statistical error is increasingly dominant. The NLO QCD fit gives a good description of the measured data, namely the rise of the cross-section with decreasing x, which reflects the increase of the sea-quark and gluon densities.

In fig. 9 the emphasis is put on the high x region, and the reduced cross-section is shown as a function of Q^2 at fixed values of x between $x = 0.07$ and $x = 0.65$. At $x = 0.45$ some excess of the cross-section over the SM prediction is visible for the highest Q^2 values, which corresponds to the accumulation of events around an inclusive invariant mass of the lepton quark system of about 200 GeV, and which was already pointed out in the 1994 to 1996 data [13]. The significance of this excess has decreased with the enhanced statistics which includes the 1997 data. The cross-section is compared to the MRST parton density and the NLO QCD fit. At the lowest x value of 0.07, both parameterisations are in good agreement, but at higher x the new data, which are included in the QCD fit, lower the prediction from the fit by up to 5%. The direct comparison with the BCDMS measurement [48] shows the same trend: from $x = 0.28$ up to $x = 0.65$, the H1 data are slightly below the extrapolation obtained from the BCDMS data.

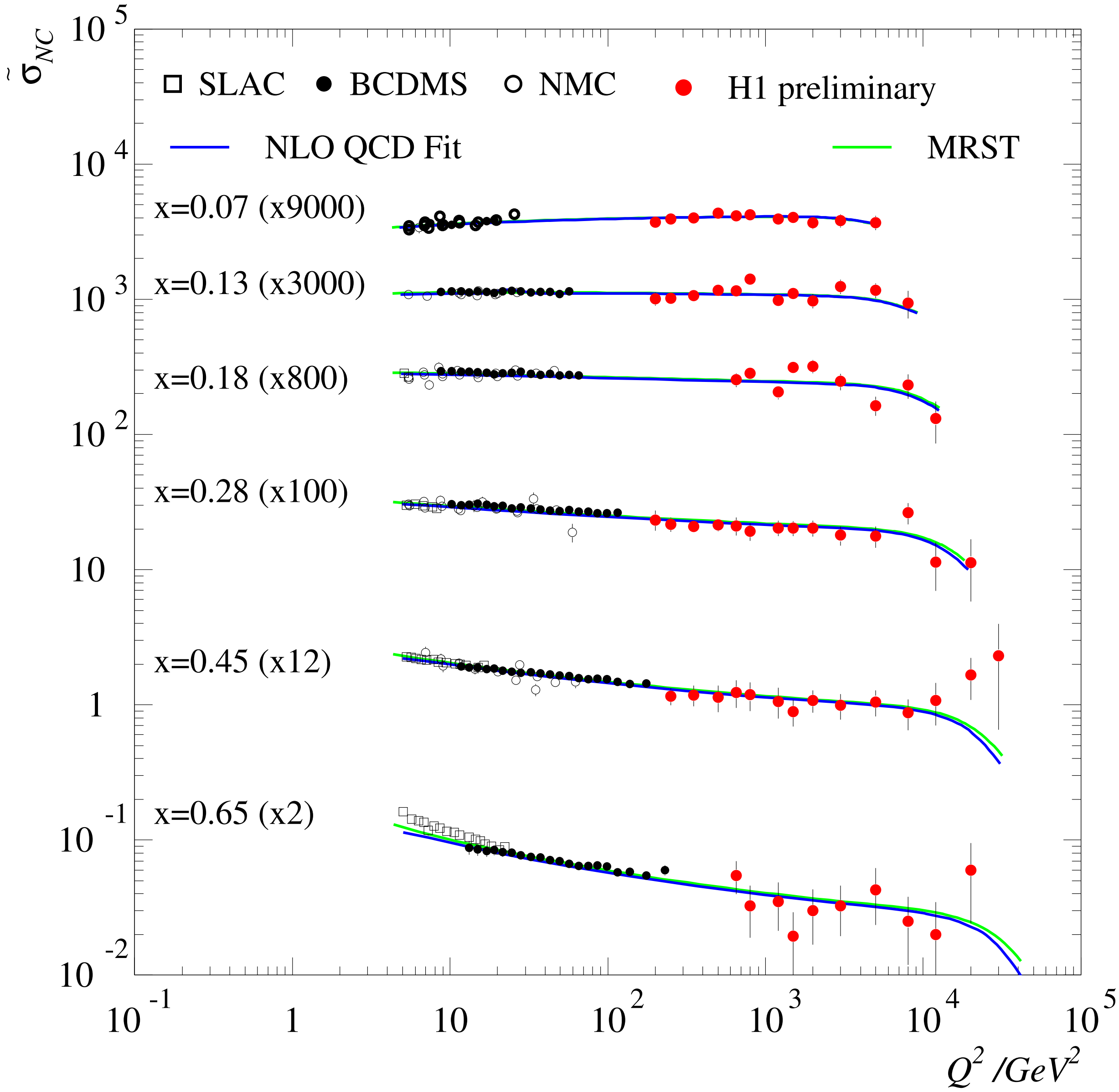

Figure 9: *The reduced neutral current cross section (as defined in eq. 13) at high x compared with Standard Model predictions from MRST and the H1 NLO QCD fit. The error bars represent the total error of the measurements.*

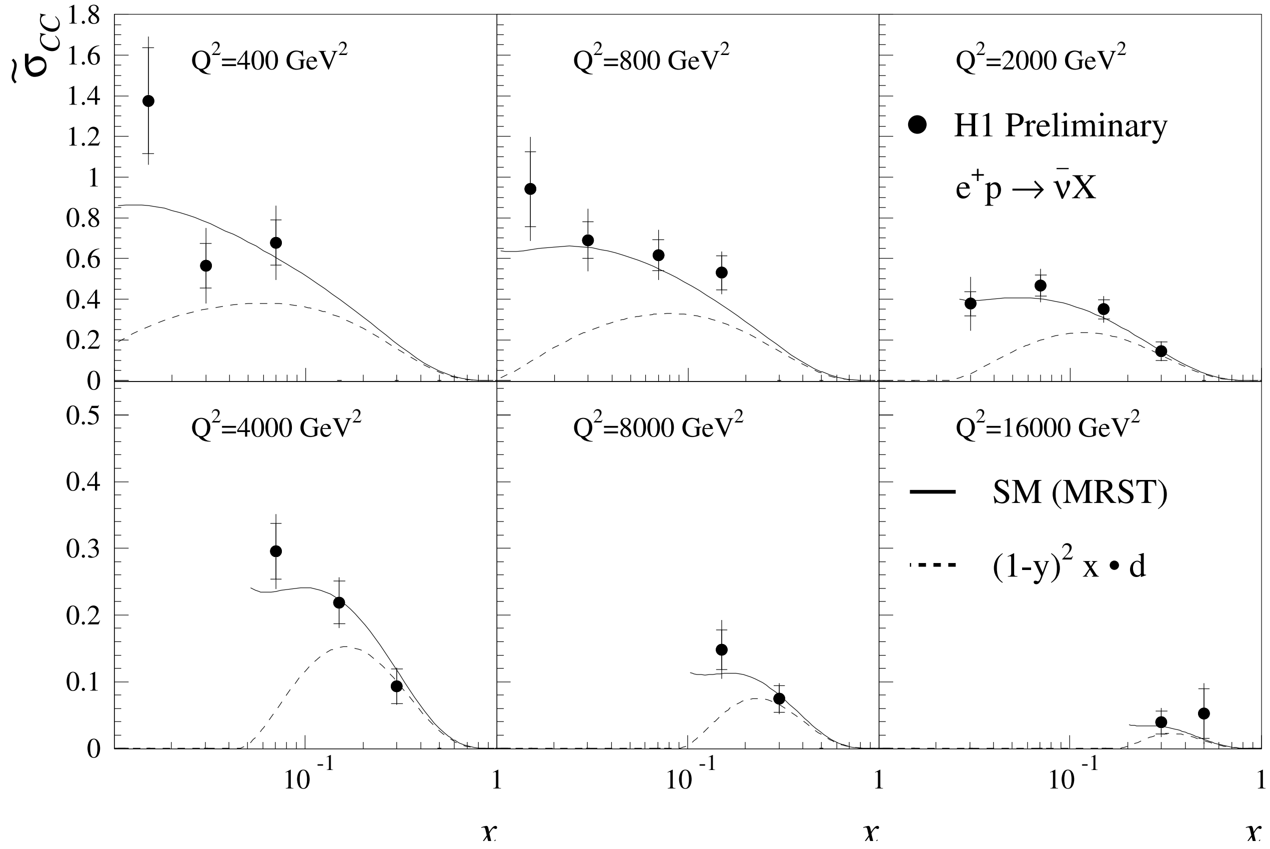

Figure 10: *The reduced charged current cross section (as defined in eq. 14) as a function of x for different Q^2 compared with the Standard Model prediction (using MRST parton distributions). Also shown is the xd contribution to it. The inner error bars represent the statistical errors, the outer ones correspond to the total error.*

The double differential CC cross-section has been measured for the first time at high Q^2 and is displayed in its reduced form in fig. 10. It is still largely dominated by the statistical error. The most important systematic error is the uncertainty on the energy scale of the hadronic final state. Within these errors, the measurement is in good agreement with the predicted cross-section from the Standard Model using the MRST [49] parton distributions. Also shown is the contribution to the cross-section of the term $(1-y)^2(xd)$ which is dominated in the Standard Model by the d valence quark at high x.

The strong suppression of the d and s contributions in the double differential CC cross-section at high y due to the $(1-y)^2$ term, and the small contribution of the sea quarks at high x, are better studied when replotting the reduced cross-section at fixed x as a function of y as can be seen in fig. 11. The relative contribution given by the MRST parametrization are also shown. As expected, the reduced cross-section grows at low y, because the $(1-y)^2$ term increases towards one, and it grows at low x because the sea quark contribution increases in this domain. At $x = 0.3$, the shape of the measured distribution, which decreases quickly towards zero, indicates that the sea quark contribution is indeed small at large x.

At $x \geq 0.3$ the cross-section is largely dominated by the d valence quark. It is therefore instructive to compare directly in the high x domain the structure function term of the NC cross-section (i.e. $Y_+\tilde{\sigma}_{NC}$) with the CC one (i.e. $\tilde{\sigma}_{CC}$) as shown in fig. 12, in particular in a region in which the γZ interference term is still small ($Q^2 \lesssim 5000$ GeV^2). At $x = 0.3$, which

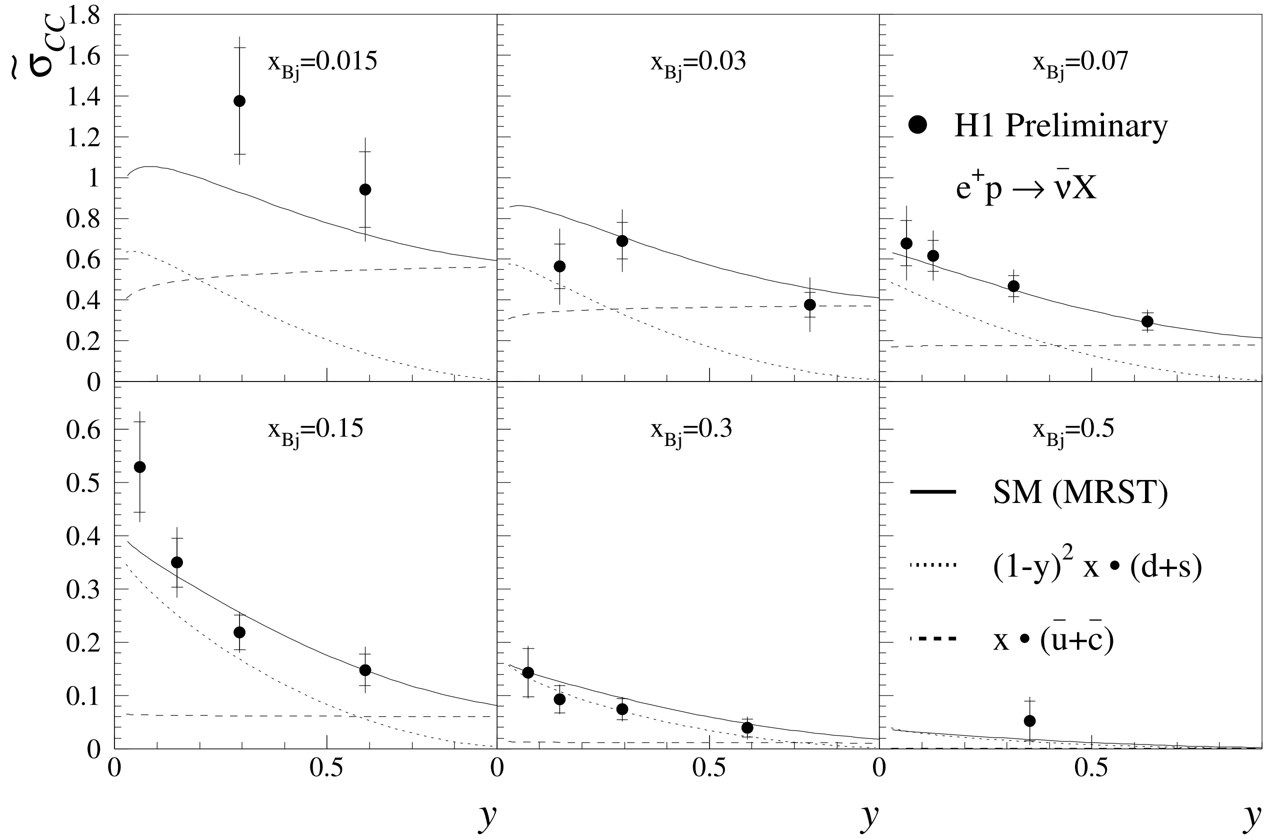

Figure 11: *Reduced double differential CC cross section (as defined in eq. 14) plotted as a function of y for different values of x, and compared to the Standard Model (MRST parton distributions). Also shown are the contributions coming from the $(d + s)$ and from the sea antiquarks. The inner error bars represent the statistical errors, the outer ones correspond to the total error.*

corresponds to $y = 0.07(0.15)$ at $Q^2 = 2000(4000)$ GeV^2, we are thus comparing in LO QCD, neglecting the small sea quark contribution,

$$[1 + (1 - y)^2] \ (\frac{4}{9}u + \frac{1}{9}d) = 0.83(0.76) \ (u + \frac{1}{4}d) \quad \text{for NC} \tag{15}$$

with

$$(1 - y)^2 \ d = 0.86(0.72) \ d \qquad \text{for CC.} \tag{16}$$

From the 2000 and 4000 GeV^2 points of fig. 10, we can thus directly observe that the u valence quark distribution is between 1.5 to 3 times larger than the d at $x = 0.3$. An analysis which aims at measuring the u/d ratio is in preparation.

3.6 Structure Function Results

Assuming the validity of perturbative QCD and the electroweak Standard Model, the proton structure function F_2^p ($\equiv F_2^{em}$) can be extracted from the double differential NC cross-section. Note that in the Standard Model the correction to obtain F_2^p from $\tilde{\sigma}_{NC}$ with this procedure is lower than 10% up to $Q^2 \approx 3000$ GeV^2. Fig. 13 shows the preliminary measurements with the

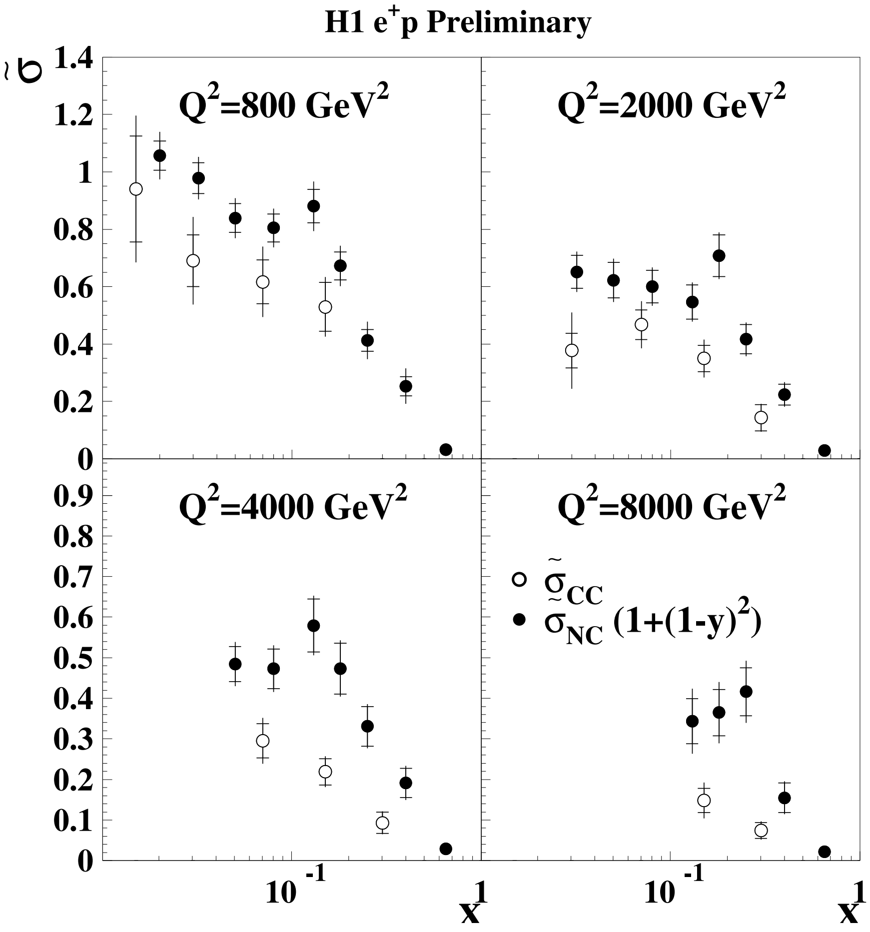

Figure 12: *Comparison of the structure function terms of the neutral and charged current double differential cross-sections (i.e. of $Y_+\tilde{\sigma}_{NC}$ and $\tilde{\sigma}_{CC}$) as a function of x in bins of Q^2. The inner error bars represent the statistical errors, the outer ones correspond to the total error.*

1994-1997 event sample at $Q^2 \geq 200$ GeV^2 presented in this paper, the published data from the 1994 data taking [7] and the "very low" Q^2 published data from the 1995 shifted vertex runs [50]. All measured data points give a consistent picture from $Q^2 \approx 1$ GeV^2 up to 30000 GeV^2. As expected from the scaling violations predicted by perturbative QCD, a positive slope as a function of Q^2 is visible for the low x data points. This slope decreases with increasing x, shows a flat behaviour at $x \approx 0.3$ and becomes slightly negative in the high x region. This behaviour is well described over the whole kinematic plane by the H1 NLO QCD fit [51] which was performed exclusively on the low Q^2 data. The consistency with the fixed target data is also established at high Q^2, in particular at $x = 0.25$ and 0.40 in which the measurements are performed in contiguous kinematic regions.

4 Standard Model Interpretation

The Standard Model predictions, which are compared to the data in section 3, rely on the parton distribution functions (pdfs) of the proton, which are not predicted by QCD and so must be obtained from the data. In order to obtain the best estimate of the pdfs two complementary approaches are taken for the NC and CC cross-section calculations. In the NC case the new

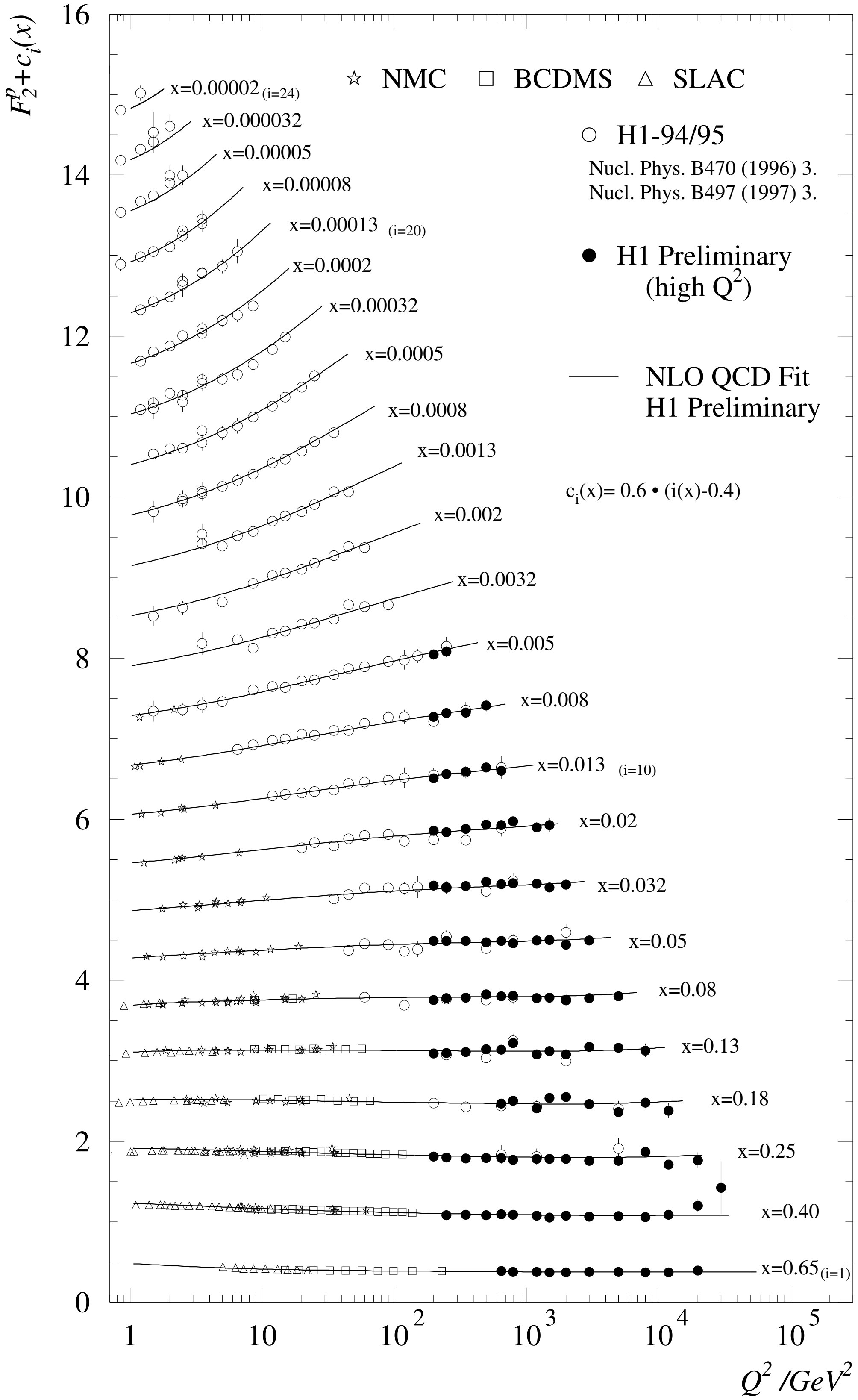

Figure 13: F_2^p ($\equiv F_2^{em}$) *results from* $Q^2 \approx$ *1 to 30000 GeV*^{2}*, and for* x *values between .00002 and 0.65, assuming* xF_3 *and* F_L *as given by the SM. The NLO DGLAP equations give a good description of the data over the kinematic range considered. The error bars represent the total error of the measurements.*

data are of such a precision as to be sensitive to small differences in the pdfs. Thus a new NLO QCD fit has been performed, including the new high Q^2 data as well as H1 and fixed target charged lepton-nucleon data at lower Q^2. For the prediction of the CC cross-section, which is sensitive to the relative contribution of the quarks and antiquarks in the proton, we use the MRST parton distributions. These pdfs are evaluated with fits that include non-DIS data which give further constraints on the flavour composition of the sea.

4.1 QCD Analysis of the Neutral Current Data

The DGLAP evolution equations[6] are solved in the next to leading order (NLO) $\overline{MS}$ factorisation scheme using the program QCDNUM[52]. To ensure that the perturbative approximation is valid a starting scale of $Q_0^2 = 4$ GeV^2 is taken at which four parton densities are parameterised. These are the up and down valence quarks (xu_v and xd_v), the gluon (xg), and the sea quark distribution (xS). The sea quark density is assumed to have equal components from quarks and anti-quarks and is defined as $xS = 2x(\bar{u} + \bar{d} + \bar{s} + \bar{c})$ at Q_0^2 where $\bar{s} = \bar{u}/2$ and $\bar{d} = \bar{u}$. Since the new data entering the fit are at high Q^2, far above the squared masses of the charm and the bottom quark, a massless approach is used within the DGLAP equations. The xb density is evolved from zero at a Q^2 threshold defined such that $xb(x, Q^2) = 0$ for $Q^2 < (5)^2\ \mathrm{GeV}^2$ and the charm component is normalised to 2% of the sea quark density at $Q^2 = Q_0^2$, which gives a good description of the H1 measurements[53] of ${F_2}^{c\bar{c}}$, the charm induced structure function. The functional forms of the parton densities are as follows:

$$
\begin{aligned}
xu_v(x, Q_0^2) &= A_u x^{B_u}(1-x)^{C_u}(1 + D_u x + E_u\sqrt{x}) \\
xd_v(x, Q_0^2) &= A_d x^{B_d}(1-x)^{C_d}(1 + D_d x + E_d\sqrt{x}) \\
xg(x, Q_0^2) &= A_g x^{B_g}(1-x)^{C_g}(1 + D_g x + E_g\sqrt{x}) \\
x\mathrm{S}(\mathrm{x}, \mathrm{Q}_0^2) &= A_S x^{B_S}(1-x)^{C_S}(1 + D_S x + E_S\sqrt{x})
\end{aligned}
$$

By applying the valence counting rules which require $\int_0^1 u_v dx$=2 and $\int_0^1 d_v dx$=1 the parameters A_u, and A_d are determined. In addition application of the momentum sum rule requiring $\int_0^1 (\sum_i (xq + x\bar{q}) + xg)dx$=1 allows the determination of one further normalisation parameter, taken to be A_g. The strong coupling constant, α_s, was fixed at the value $\alpha_s(M_Z^2) = 0.118$. The weak bosons and the top quark masses were fixed at the values of $M_Z = 91.175$ GeV, $M_W = 80.20$ GeV, $M_H = 100$ GeV and $M_{top} = 175$ GeV. The fine structure constant was set to the value of $\alpha = 1/137.036$.

In addition to the new measurements of the NC cross-sections, F_2 data from NMC[54] and BCDMS[48] on both proton and deuteron targets were included in the fit in order to constrain the parton densities at high x. In the region of the fixed target data, high x and low Q^2, target mass effects and higher twists may have a large influence. Therefore in order to reduce these effects all the data used were required to have $Q^2 > 4$ GeV^2, $W^2 \geq 10$ GeV^2 as well as $Q^2 \geq 15$ GeV^2 for $x \geq 0.5$. In addition the F_2 data from H1[7] were included for $Q^2 \leq 120$ GeV^2 as well as the preliminary low Q^2 measurements from the H1 95/96 analysis [51]. The normalisations of all data sets were left free within the quoted luminosity uncertainty taking into account their correlations. The fits were performed using the program MINUIT[55] which minimised the χ^2 defined with statistical and uncorrelated systematic errors added in quadrature. In order to assess the agreement of the high Q^2 NC data with the prediction of perturbative QCD two fits were performed. The first fit excluded the new H1 high

Q^2 data and was extrapolated into the high Q^2 region[9], whilst the second included all the data. Both fits provide a good description of all data sets and have $\chi^2/\mathrm{ndf} \approx 1.2$ (the ndf for the two fits are 875 and 1003).

4.2 Test of the W propagator term

Since the process $e^+p \to \nu_e X$ proceeds via the t channel exchange of a virtual W boson, the value of M_W extracted from the propagator term is a direct measurement of the W mass in the spacelike regime. It is a test of the Standard Model to compare such a measurement with timelike and indirect determinations from other experiments.

In the double differential CC cross section at the tree level, which is given in eq. 11, the first term, G_F, is precisely known from measurements of muon decay: $G_{F,exp} = 1.16639 \times 10^{-5}\ \mathrm{GeV}^{-2}$ [56]. The Q^2 dependence of this cross section is determined by the propagator term, $M_W^2/(Q^2 + M_W^2)$, given the known Q^2 dependence in the structure function term (the QCD evolution of the pdfs and the known helicity factor $1 - y = 1 - Q^2/sx$). In order to construct a fit of the CC cross-section that is sensitive predominantly to the value of M_W in the propagator term, the following χ^2 function is minimised:

$$\chi^2 = \sum_{i=1}^{n} \left[\frac{(T_i - E_i)}{\delta E_i} \right]^2 \tag{17}$$

with

$$E_i = \frac{1}{G_{F,exp}^2} \left(\frac{d^2\sigma_{CC}}{dxdQ^2} \right)_i \qquad \text{and} \qquad T_i = \frac{1}{G_{F,SM}^2(\vec{p})} \left(\frac{d^2\sigma_{CC}}{dxdQ^2} \right)_i \tag{18}$$

E_i is the measured cross-section for the data point i divided by the square of the experimental value of G_F, and δE_i is the quadratic sum of the statistical and uncorrelated errors. T_i is the equivalent quantity to E_i predicted in the Standard Model, divided by the square of the Standard Model value $G_{F,SM}(\vec{p})$, thereby cancelling the M_W dependence of the G_F^2 term in the cross-section. T_i is calculated using as input the quantities $\vec{p} = (\alpha, M_W, M_Z, M_{top}, M_H)$ and the parton distribution functions from MRST. The values of α, M_Z, M_{top} and M_H are specified in section 4.1 and M_W is allowed to vary in the fit.

The best value obtained from minimizing the χ^2 function yields

$$M_W = 81.2 \pm 3.3(\mathrm{stat.}) \pm 4.3(\mathrm{syst.})\mathrm{GeV} \tag{19}$$

with $\chi^2/\mathrm{ndf} = 18.2/17$. The main contribution to the systematic error arises from the $3 - 4\%$ uncertainty in the LAr hadronic energy scale. There is an additional 2.8 GeV theoretical uncertainty on the result which arises from the effect of different pdfs, and from the 4% uncertainty in the radiative corrections (see section 3.3).

The value of M_W extracted by this method is found to be insensitive to changes in the values assumed for M_H and M_{top} and is in agreement with both direct and indirect determinations measurements performed in other channels [57].

[9] It is called NLO QCD fit ($Q^2 \leq 120\ \mathrm{GeV}^2$) in fig. 6a.

5 Summary

Neutral and charged current processes with Q^2 between 200 and 30000 GeV^2 have been studied in e^+p collisions with the H1 detector at HERA using the data taken in 1994-1997.

The single differential cross-section $d\sigma/dQ^2$ has been measured in NC and CC and is shown to be in good agreement with the Standard Model predictions. A slight excess at $Q^2 \geq 15000$ GeV^2 is visible, but with less significance than using the 1994-1996 data alone.

The NC single differential cross-section $d\sigma/dx$ has been measured for $Q^2 \geq 1000$ and 10000 GeV^2. The measurements are in agreement with the SM prediction. For $Q^2 \geq 10000$ GeV^2, there is disagreement at the 3 σ level when the effects of the Z exchange are removed.

The double differential cross-sections $d^2\sigma/dxdQ^2$ have been measured for NC and for CC interactions. For NC, the data are well described by a NLO QCD fit performed with the new NC high Q^2 data together with the low Q^2 HERA data and fixed target data. The inclusion of the new NC high Q^2 points has been shown to reduce the prediction from the fit of the low Q^2 data alone by up to 5% at the highest measured $x = 0.65$. The double differential CC cross-section is in agreement with the SM prediction but the precision of the measurement is still statistically limited. The expected contributions of valence and sea quarks can be seen in the measured kinematic domain. A comparison of the NC and CC double differential cross-sections at high x illustrates the possibility of measuring the u/d ratio in the valence region with the present data.

A fit to the Q^2 dependence of the CC double differential cross-section gives a propagator mass $M_W = 81.2 \pm 5.4$ GeV. A fit to the Q^2 dependence of the CC double differential cross-section gives a propagator mass $M_W = 81.2 \pm 5.4$ GeV. This value agrees well with measurements of the mass of the W boson in processes where it is directly produced, thereby confirming the electroweak sector of the Standard Model in space-like lepton nucleon scattering.

Acknowledgements

We are grateful to the HERA machine group whose outstanding efforts have made and continue to make this experiment possible. We thank the engineers and technicians for their work in constructing and now maintaining the H1 detector, our funding agencies for financial support, the DESY technical staff for continual assistance, and the DESY directorate for the hospitality which they extend to the non-DESY members of the collaboration.

References

[1] E.D. Bloom et al., Phys. Rev. Lett. **23** (1969) 930.
M. Breidenbach et al., Phys. Rev. Lett. **23** (1969) 935.

[2] Gargamelle Neutrino Collab., F.J. Hasert, et al., Phys. Lett. **B46** (1973) 138.

[3] H1 Collab., T. Ahmed et al., Phys. Lett. **B324** (1994) 241.

[4] H1 Collab., I. Abt et al., Nucl. Phys. **B407** (1993) 515.
H1 Collab., T. Ahmed et al., Nucl. Phys. **B439** (1995) 471.

[5] ZEUS Collab., M. Derrick et al., Phys. Lett. **B316** (1993) 412.
ZEUS Collab., M. Derrick et al., Z. Phys. **C65** (1995), 379.

[6] Yu. L. Dokshitzer, Sov. Phys. JETP **46** (1977) 641;
V. N. Gribov and L.N. Lipatov, Sov. J. Nucl. Phys. **15** (1972) 438 and 675;
G. Altarelli and G. Parisi, Nucl. Phys. **B126** (1977) 297.

[7] H1 Collab., S. Aid et al., Nucl. Phys. **B470** (1996) 3.

[8] ZEUS Collab., M. Derrick et al., Z. Phys. **C72** (1996) 399.

[9] H1 Collab., S. Aid et al., Z. Phys. **C67** (1995) 565.

[10] ZEUS Collab., M. Derrick et al., Phys. Rev. Lett. **75** (1995) 1006.

[11] H1 Collab., S. Aid et al., Phys. Lett. **B379** (1996) 319.

[12] ZEUS Collab., M. Derrick et al., Z. Phys. **C72** (1996) 47.

[13] H1 Collab., C. Adloff et al., Z. Phys **C74** (1997) 191.

[14] ZEUS Collab., J. Breitweg et al., Z. Phys. **C74** (1997) 207.

[15] A.Blondel, F.Jacquet, Proceedings of the Study of an ep Facility for Europe,
ed. U.Amaldi, DESY 79/48 (1979) 391.

[16] U. Bassler and G. Bernardi, Nucl. Instr. Meth. **A361** (1995) 197.

[17] U. Bassler and G. Bernardi, DESY 97-137 (1997) *subm. to Nucl. Instr. Meth.*

[18] S. Bentvelsen et al., Proceedings of the Workshop Physics at HERA, vol. 1,
eds. W.Buchmüller, G.Ingelman, DESY (1992) 23.
C. Hoeger, ibid., 43.

[19] H1 Collab., I. Abt et. al., Nucl. Instr. Meth. **A386** (1997) 310 and 348.

[20] H1 Calorimeter Group, B. Andrieu et al., Nucl. Instr. Meth. **A336** (1993) 460.

[21] H1 Spacal Group, R.D. Appuhn et al., Nucl. Instr. Meth. **A386** (1997) 397.

[22] H1 Collab., Luminosity Measurement in the H1 Experiment at HERA,
ICHEP 96-Warsowie, pa17-026.

[23] G. A. Schuler and H. Spiesberger, Proceedings of the Workshop Physics at HERA, vol. 3,
eds. W. Buchmüller, G. Ingelman, DESY (1992) 1419.

[24] A. Kwiatkowski, H. Spiesberger and H.-J. Möhring, Comp.Phys.Comm. **69** (1992) 155.

[25] G. Ingelman, Proceedings of the Workshop Physics at HERA, vol. 3,
eds. W. Buchmüller, G. Ingelman, DESY (1992) 1366.

[26] L. Lönnblad, Comp.Phys.Comm. **71** (1992) 15.

[27] R. Brun et al., GEANT3 User's Guide, CERN-DD/EE-84-1 (1987).

[28] A.D Martin, W.J. Stirling and R.G. Roberts, Phys. Lett. **B306** (1993) 145; **B309** (1993).

[29] T. Sjöstrand, CERN-TH-7112/93 (1993).

[30] T.Sjöstrand, CERN-TH-6488/92 (1992), Comp.Phys.Comm.**82** (1994) 74.

[31] A. Coureau and P. Kessler, Phys. Rev. **D46** (1992) 117.

[32] S. Barnov et al, Proceedings of the Workshop Physics at HERA, vol. 3, eds. W. Buchmüller, G. Ingelman, DESY (1992) 478.
J.A.M. Vermaseren, Nucl. Phys. **B229** (1983) 347.

[33] U. Bauer, J.A.M. Vermaseren and D. Zeppenfeld, Nucl. Phys. **B375** (1992) 3.

[34] G. Martin, Ph.D. Thesis, Hamburg (1997).

[35] H1 Collab., C. Adloff et al., DESY 98-063 (1998) *subm. to Eur.Phys.J.*

[36] E. Chabert, Ph.D. Thesis, Marseille *in preparation*.

[37] B. Heinemann, Ph.D. Thesis, Hamburg *in preparation*.

[38] I. Negri, Ph.D. Thesis, Marseille (1998).

[39] H1 Calorimeter Group, B. Andrieu et al., Nucl. Instr. Meth. **A350** (1994) 57.

[40] H1 Calorimeter Group, B. Andrieu et al., Nucl. Instr. Meth. **A336** (1993) 499.

[41] U. Bassler and G. Bernardi, Z. Phys. **C76** (1997) 223.

[42] H.P. Wellisch et al., MPI-PhE/94-03 (1994).

[43] D.Yu. Bardin et al., Z. Phys. **C42** (1989) 679.

[44] H. Spiesberger, Nucl. Phys. **B349** (1991) 109.

[45] A. Arbuzov et. al., DESY 95-185 (1995).

[46] H. Spiesberger et al., Proceedings of the Workshop Physics at HERA, vol. 2, eds. W.Buchmüller, G.Ingelman, DESY (1992) 798.

[47] H1 Collab., A Search for Leptoquark Bosons in DIS at High Q^2 at HERA, ICHEP 98-Vancouver, 98-580 (1998).

[48] BCDMS Collab., A. Benvenuti et al., Phys. Lett. **B223** (1989) 485.

[49] A. Martin et al., RAL-TR-98-029.

[50] H1 Collab., C. Adloff et al., Nucl.Phys. **B497** (1997) 3.

[51] H1 Collab., A Measurement of the Inclusive Deep Inelastic ep Scattering Cross Section at low Q^2 at HERA, IECHEP 97-Jerusalem, 97-260 (1997).

[52] Source code available on request by email to Botje@nikhef.nl

[53] H1 Collab., C. Adloff et al., Z. Phys. **C72** (1996) 593.

[54] NMC Collab., M. Arneodo et al., Phys. Lett. **B364** (1995) 107.

[55] F. James, CERN Program Library, D506.

[56] PDG 98, Eur. Phys. J. **C3** (1998) 1.

[57] CDF Collab., F. Abe et al., Phys. Rev. Lett. 75, (1995) 11; Phys.Rev. **D 52** (1995) 4784.
DØ Collab., B. Abbott et al., FERMILAB PUB-97/422-E (1997) *subm. to Phys.Rev.*
ALEPH Collab., R. Barate et al., Phys. Lett. **B422** (1998) 384.
DELPHI Collab., P. Abreu et al., Eur.Phys.J. **C2** (1998) 581.
L3 Collab., M. Acciarri et al., Phys. Lett. **B413** (1997) 176.
OPAL Collab., K. Ackerstaff et al., Eur.Phys.J. **C1** (1998) 395.